International Journal of Greenhouse Gas Control 108 (2021) 103313

Contents lists available at ScienceDirect

International Journal of Greenhouse Gas Control

journal homepage: www.elsevier.com/locate/ijggc

Acoustic and optical determination of bubble size distributions – Quantification of seabed gas emissions

Jianghui Li [a,*], Paul R. White [a], Ben Roche [b], Jonathan M. Bull [b], Timothy G. Leighton [a], John W. Davis [b], Joseph W. Fone [b,c]

[a] Institute of Sound and Vibration Research, University of Southampton, Southampton SO17 1BJ, UK
[b] Ocean and Earth Science, University of Southampton, National Oceanography Centre, Southampton SO14 3ZH, UK
[c] Bullard Laboratories, University of Cambridge, Cambridge CB3 0EZ, UK

ARTICLE INFO

Keywords:
Bubbles
Identification
Underwater acoustics
Greenhouse gas
CO_2
Marine Carbon Capture and Storage
CCS

ABSTRACT

Passive acoustic techniques can be used to identify and quantify underwater gas release at natural sites, or at locations related to anthropogenic activities. There are still significant issues in extracting bubble signals from background noise, particularly for bubble counting and sizing techniques relying on inversion of the time-averaged acoustic spectrum. In this work we propose an adaptive single bubble identification technique, which incorporates bubble acoustic characteristics including pulsation time interval, frequency bandwidth and radiation strength. The method applies a cross-spectrogram, enabling an increase in signal-to-noise ratio resulting in a reduction of the false alarm rate on bubble identification. We demonstrate this technique using an array of hydrophones to determine the bubble size distribution and gas flux at a controlled CO_2 release site, 4 m beneath the seabed, at 120 m water depth in the central North Sea. The results show that the bubble radius, as estimated using acoustics has a distribution with a peak in the 0.15–0.3 cm range, while an estimate based on optical method suggests a range of 0.2–0.5 cm. The gas flux is acoustically estimated as 32–88 kg/day in response to a known gas injection flow rate 143 kg/day, indicating 22–62% of the injected CO_2 is emitted from the seabed in gaseous form, with the remainder being trapped, or dissolved.

1. Introduction

In recent years, carbon dioxide capture and storage (CCS) in the marine environment has been acknowledged as an important strategy to mitigate greenhouse gas emissions and slow down global temperature rises and ocean acidification (Pachauri et al., 2014; Roelofse et al., 2019; Caserini et al., 2017; Vielstädte et al., 2019). Proving the ability to demonstrate the integrity of a CCS reservoir is a vital element of assurance monitoring, e.g. developing *in situ* continuous and autonomous monitoring techniques (Loewen and Melville, 1991; Leighton and White, 2011; Blackford et al., 2015; Mabon et al., 2014; Hvidevold et al., 2016; Bergès et al., 2015; Atamanchuk et al., 2015; Taylor et al., 2015; Cevatoglu et al., 2015; Shitashima et al., 2015; Kolster et al., 2018; Stork et al., 2018; Kita et al., 2015). Recent technology developments for such monitoring include innovative methods in terms of acoustics, optics, chemistry, biology and geophysics (Shitashima et al., 2015; Li et al., 2019a, 2019b; Jenkins et al., 2012; Stalker et al., 2012; Zoback and Gorelick, 2012; Johnson et al., 2009; Roberts et al., 2017; Blackford et al., 2015). In acoustics, both active (Nikolovska et al., 2008; Leblond et al., 2014; Leifer and Tang, 2007; von Deimling et al., 2011; Sarıtaş et al., 2018; Rychert and Weber, 2020) and passive (Leighton and White, 2011; Bergès et al., 2015; Li et al., 2019a; Dziak et al., 2018) methods have been applied to understand gas seeps within the water column; these techniques complement each other with active methods being most effective at localisation and imaging (von Deimling et al., 2010; Hovland and Sommerville, 1985), with passive techniques providing the ability for quantifying fluxes over extended time periods (Li et al., 2019a).

The effectiveness of passive acoustic monitoring techniques in the context of a controlled CO_2 gas release experiment was demonstrated in the QICS (Quantifying and Monitoring Potential Ecosystem Impacts of Geological Carbon Storage) project conducted off the west coast of Scotland (Bergès et al., 2015). Further, it has been applied to the monitoring of natural gas seeps (Li et al., 2019a; Leifer and Tang, 2007). In previous studies a single hydrophone attached to an acoustic recorder has been used to measure the sounds of bubbles emerging from the

* Corresponding author.

https://doi.org/10.1016/j.ijggc.2021.103313
Received 10 July 2020; Received in revised form 22 February 2021; Accepted 4 March 2021
Available online 7 April 2021

seabed. Leighton and White (2011) proposed the use of an inversion algorithm on the measured sound in a frequency range of interest to identify the CO_2 gas release from seeps. In both the gas-controlled (Bergès et al., 2015; Blackford et al., 2014) and natural field experiments (Li et al., 2019a; Li et al., 2020; Leifer and Tang, 2007), their passive acoustic technique has been demonstrated to be effective and economic for CCS leakage monitoring.

There are two approaches to estimate the bubble size distribution using passive acoustic data. Firstly, when the rate of bubble generation is low, so that the sounds of individual bubbles formed do not overlap in time and frequency, then individual bubble formation events can be counted and the size of each bubble determined using the dominant frequency emitted (Leighton and Walton, 1987). This approach requires automatic detection of bubble signals from ambient background noise. The main challenge with this approach is the selection of a detection criterion which will inevitably involve a trade-off between avoiding false positives (mistaking noise for a bubble) and false negatives (failing to detect a bubble), especially in low signal-to-noise ratio (SNR) environment. The second approach (Loewen and Melville, 1991; Leighton and White, 2011) is designed to operate in higher gas flux conditions, when bubble signatures overlap, so individual bubble emissions cannot be isolated. This technique is based on measurements across the frequency band of interest, which is assumed to be dominance by the bubble sounds across the band of interest. An inversion method can be applied to the resulting spectrum for inferring the bubble size distribution. To realise this approach, the spectral method requires quantification of the average source level for a bubble emission as a function of bubble radius. This level is expected to vary with bottom type, water depths, trace element concentrations (e.g. surfactants) and leads to estimates with significant uncertainties. Ambient noise can be misinterpreted as sound arising from bubbles, which would inflate the estimated bubble size distribution. To reduce this uncertainty, the frequency band over which bubble sounds dominate over the noise needs to be identified, and if necessary, the spectrum of the ambient noise needs to be subtracted from the measured signal spectrum. The frequency band over which the bubble sounds dominants will reduce as the SNR reduces and that will restrict the range of bubble radii over which the bubble size distribution can be estimated.

Combining the data from multiple hydrophones via beamforming can enhance the performance of both passive quantification methods. Beamforming produces an enhancement in SNR by creating a system with directivity, which rejects noise arriving from directions other than those associated with the known direction to the source. The SNR enhancement depends on the array elements and varies as a function of frequency. A conventional beamformer (CBF), sometimes called a delay and sum beamformer, provides a well-established and robust method for enhancing a spatially localised source such as a single stream of bubbles. However, when there is a distributed source of sound, for example an area with several seeps close together, the beamforming becomes problematic without using a sufficiently large array to resolve each of the seeps across the full frequency range. Specifically, in a scenario of closely spaced seeps, the energy from adjacent seeps may be detected

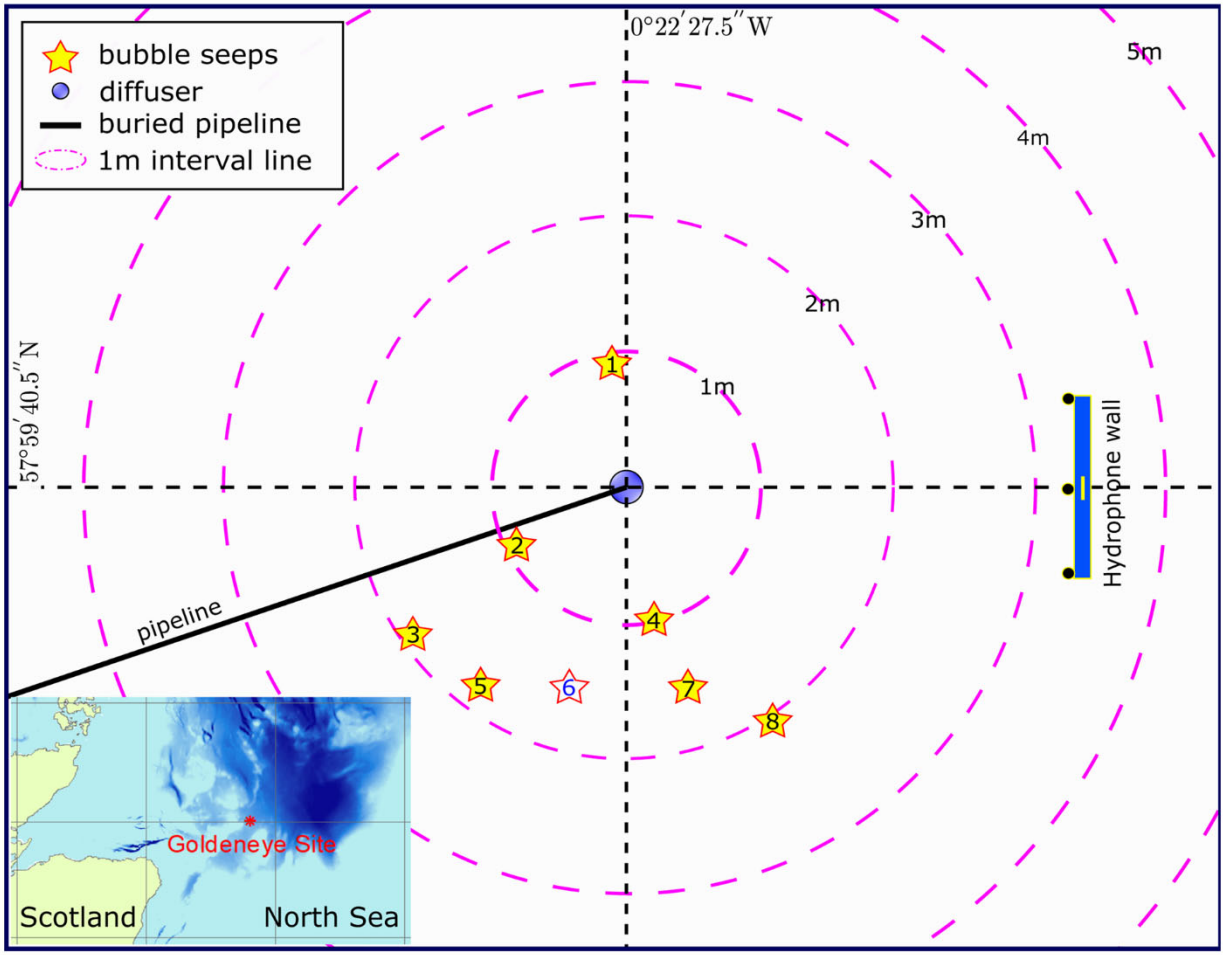

Fig. 1. Mapped (plan view) gas seep locations when the CO_2 release rate was 143 kg/day (50 L/min standard temperature and pressure (STP)) and hydrophone wall placement. The central dot is marked as the coordinate above the tip of the gas diffuser; stars represent eight observed gas seeps, and seep 6 is the one where the optical quantification is performed. The hydrophone wall was placed at 3.3 m east from the central point. Concentric dashed circles (magenta) show distances from experiment epicentre in metres. The inset map shows the location of the experiment in the North Sea.

and potentially misallocated to the seep being focused on. This misallocation is a common problem affecting both passive acoustic methods, and is more likely to occur at lower frequencies where the beamformer has a lower directivity.

In this paper, we propose an adaptive single bubble identification technique based on recordings from an array of hydrophones. Rather than applying a conventional beamformer, this work employs a method based on a cross-spectrogram. We demonstrate the technique with data collected from a controlled CO_2 gas release experiment conducted as a part of the project STEMM-CCS (Strategies for Environmental Monitoring of Marine Carbon Capture and Storage) in the central North Sea at the depth of 120 m. In the experiment, we deployed a hydrophone array to collect the sound data associated with the bubble release, along with an optical frame to collect video data. Fig. 1 shows a plan view of the study area, where a buried pipe releases CO_2 gas into the seabed (the pipe outlet being approximately 4 m under the seabed). The gas was observed to emerge from the seabed, and enter the water column at eight distinct locations when the continuous injection rate was 143 kg/day. Fig. 1 shows the actual location of these seeps with respect to the pipe and the hydrophone array, which consists of five hydrophones arranged in an X configuration. Field results are used to illustrate the potential of the identification technique applied to marine gas leakage monitoring (see Flohr et al., 2020b for a full description of the STEMM-CCS release experiment).

This paper is organised as follows. We describe the theoretical framework in Section 2 and the proposed acoustic identification technique in Section 3. An optical bubble identification method used for comparison is presented in Section 4. The controlled STEMM-CCS gas release experiment and the deployment of an array of five hydrophones and an optical frame are detailed in Section 5, followed by investigation results of the proposed techniques applied on the data recorded from the experiment in Section 6. Finally, Section 7 draws some conclusions.

2. Theoretical framework

The processing of acoustic data from arrays of hydrophones is well-established (Van Trees, 2004; Li et al., 2016; Li, 2017; Li and Zakharov, 2018). The most commonly considered approach is to use a CBF, defined as

$$y(t) = \sum_{k=1}^{K} w_k x_k(t - v_k), \tag{1}$$

where K is the number of hydrophones, w_k are fixed weights used to shade the array, x_k [μPa] are received acoustic signals by hydrophones, t [s] is the time instant, and v_k are delays used to steer the array, i.e. control the direction in which the array "looks". This creates a beamformed signal $y(t)$ [μPa] which has directivity, in that sources in different locations make different contributions to this output. SNR can be increased by rejecting sounds from directions which are not associated with the source of interest. This directivity depends on the location of the sources and their frequency, and a CBF is less directional for low frequency sounds as compared to high frequencies. Defining the sound speed and the location of a seep relative to an array facilitates the targeting of an individual seep by steering the array.

We developed an alternative inversion approach to analyse the array of hydrophones deployed in the STEMM-CCS project. The inversion method only requires an estimate of the spectrum of the bubble signature, whereas the CBF constructs an estimate of the time series from a seep.

To develop this method we consider an array of hydrophones, placed in the vicinity of a seep producing an acoustic signal $\beta(t)$ [μPa] as measured at a distance of 1 m from the centre of the seep. Assuming spherical spreading and a constant sound speed c [m/s], then the bubble acoustic signal measured on the kth hydrophone, $x_k(t)$ [μPa], can be expressed as

$$x_k(t) = \frac{\beta(t - \tau_k)}{R_k} + n_k(t), \tag{2}$$

where $\tau_k = R_k/c$ is the delay [s] from the bubble source due to acoustic propagation, R_k [m] is the distance from the seep to the kth hydrophone, and $n_k(t)$ [μPa] is the noise on the kth hydrophone involving any other acoustic contribution apart from the bubble signal. The range for each hydrophone is great enough that the amplitudes of the signals on each hydrophone are approximately equal.

Fourier transforming (2), we obtain

$$X_k(f) = e^{-2\pi i f \tau_k} B(f) + N_k(f), \tag{3}$$

where f [Hz] represents frequency. The cross-spectrum, $S_{kl}(f)$, between the kth and lth hydrophone:

$$\begin{aligned} S_{kl}(f) &= \mathrm{E}[X_k(f)^* X_l(f)] \\ &= \mathrm{E}[(e^{-2\pi i f \tau_k} B(f) + N_k(f))^* (e^{-2\pi i f \tau_l} B(f) + N_l(f))] \\ &= e^{-2\pi i f(\tau_l - \tau_k)} \mathrm{E}[|B(f)|^2] + e^{2\pi i f \tau_k} \mathrm{E}[B(f)^* N_l(f)] + e^{-2\pi i f \tau_l} \mathrm{E}[B(f) N_k(f)^*] \\ &\quad + \mathrm{E}[N_k(f)^* N_l(f)], \end{aligned} \tag{4}$$

where $E[\cdot]$ denotes the expectation operator, and $\{\cdot\}^*$ denotes complex conjugation. Assuming the bubble signals and the background noise are uncorrelated, the second and the third terms in (4) are zero:

$$\mathrm{E}[B(f)^* N_l(f)] = E[B(f) N_k(f)^*] = 0, \tag{5}$$

and we simplify the equation as

$$S_{\mathrm{kl}}(f) = e^{-2\pi i f(\tau_l - \tau_k)} \mathrm{E}[|B(f)|^2] + \mathrm{E}[N_k(f)^* N_l(f)]. \tag{6}$$

If we assume the noise received by the two hydrophone elements are also uncorrelated, i.e. $\mathrm{E}[N_m(f)^* N_n(f)] = 0$, then we can further simplify the equation as

$$S_{kl}(f) = e^{-2\pi i f(\tau_l - \tau_k)} \mathrm{E}[|B(f)|^2], \tag{7}$$

and

$$|S_{kl}(f)| = \mathrm{E}[|B(f)|^2]. \tag{8}$$

In such case, the level of uncorrelated noise can be reduced from the operation. Therefore, the magnitude of the cross-correlation between two hydrophones is an estimate of the spectrum of the bubble signature. For an array with K hydrophone elements, there are $K \times (K-1)/2$ unique hydrophone pairs, yielding $K \times (K-1)/2$ different estimates of the cross-correlation. Since each is an estimate of the bubble spectrum these can be averaged to further reduce the noise.

3. Acoustical bubble identification

At high flow rates, bubble formation creates sounds as a continuous stationary random process. Conversely, at low flow rates the sound is characterised by a sequence of distinct short duration transient events. These two conditions suggest different approaches for estimating the cross-spectra as defined in Loewen and Melville (4). In the case of high flow rates, the assumed stationarity of the processes can be explored using a direct or indirect approach to compute the cross-spectrum (Bendat and Piersol, 2011). At low flow rates, where the signal is non-stationary, adopting a methodology based on time-frequency analysis is an appropriate approach (Hammond and White, 1996). The data collected during the STEMM-CCS experiment contained distinct transients from each bubble release event that can be classified as a low flow rate process.

3.1. Cross-spectrogram computation

The signature of each bubble is a transient event typically lasting

about ten exponentially decaying sinusoid cycles of the bubble's resonant frequency (e.g. 5 ms for a bubble sound at 2 kHz). However, after some period of time, depending on the SNR, the bubble signal is swamped by the ambient non-bubble signals. This section considers the extension of the principles described in Section 2 to a time-frequency paradigm to develop a cross-spectrogram.

The discrete time series of the received acoustic signals is firstly divided into overlapping segments $x_{p,k}(n)$, which represents the data in the pth segment on the kth hydrophone channel with 50% overlap. A windowing function, in our case a Hamming window, is applied to each segment before a fast Fourier transform (FFT) is used to compute the Fourier representation of the data $X_{p,k}(f)$. If the length of the segment is L_p and the start of each segment is S_p samples after the preceding segment, then the pth segment starts at sample number $p \times S_p$ and the centre of the segment is $pS_p + \frac{L_p}{2}$. The length of a segment L_p should be set to correspond to approximately 5 ms which represents a typical length of a bubble signature. In our case, the sample rate is 96 kHz, so that a segment length of 512 samples should be set to match approximately 5 ms, representing typical duration of a bubble signature.

The cross-spectrogram between the kth and lth channels for the pth segment can be computed as

$$C_{k,l}(p,f) = |X_{p,k}(f)^{*} X_{p,l}(f)|, \tag{9}$$

where $X_{p,l}(f)$ is the Fourier representation of data in the lth hydrophone channel. We are particularly interested in the centre frequency of the bubble sound, so the FFT was zero padded to give a higher density of frequency samples, specifically the spacing between frequency samples was 10 Hz. Following the principles in Section 2, the cross-spectrogram is averaged across all possible pairs of hydrophones in the array:

$$\overline{C}(p,f) = \frac{2}{K(K-1)} \sum_{k=1}^{K-1} \sum_{l=k+1}^{K} C_{k,l}(p,f). \tag{10}$$

The $\overline{C}(p,f)$ is an average cross-spectrogram for the pth segment at the frequency bin f.

In order to detect the individual bubble signatures we compare the cross-spectrogram to a long-term median of $\overline{C}(p,f)$. For any length data, we perform the processing on data blocks of 5 s duration. We consider the background noise as stationary and estimate the noise in each block, so the system remains adaptive to changes in the noise spectrum. Consider a block of data containing P segments with each segment 5 ms. First, the cross-spectrogram is expressed on a logarithmic scale [dB re 1 μPa^2/Hz], $\overline{C}_{\mathrm{dB}}(p,f) = 10log_{10}\overline{C}(p,f)$, then the median across the block is computed:

$$\overline{C}(f) = \frac{1}{P} \sum_{p=1}^{P} \overline{C}_{\mathrm{dB}}(p,f). \tag{11}$$

This allows a normalised cross-spectrogram to be computed as

$$\widehat{C}(p,f) = \overline{C}_{\mathrm{dB}}(p,f) - \overline{C}(f), \tag{12}$$

which forms the basis of our bubble identification method.

3.2. Bubble characteristics application

After the computation of the normalised cross-spectrogram described in Section 3.1, individual bubble sounds are detected. To achieve this, an adaptive thresholding process is applied to the cross-spectrogram. The adaptive single bubble identification algorithm is shown in Appendix A. In the algorithm, we consider both the energy threshold and the frequency bandwidth threshold on the cross-spectrogram for identifying bubble pulses.

3.2.1. Thresholding

For each frequency, local peaks in the normalised cross-spectrogram are first identified and those above a defined energy threshold, $\mathrm{Th}_{\mathrm{eng}}$ [dB], are retained. Once the peaks have been identified for each frequency, then peaks which in adjacent bins are linked together to form patches. For each segment, the index of identified peaks are recorded in a vector Q. The difference in the minimum and maximum frequency in a patch is a measure of bandwidth and this must exceed some threshold denoted by $\mathrm{Th}_{\mathrm{band}}$ [Hz], in order to be recognised as the sound from a bubble. This eliminates isolated peaks generated from noise for example. For a damped oscillator, the number of radians required for the energy to decay by e^{-1} defines the quality-factor (Leighton, 1994). The quality-factor is 18.5 for a resonance frequency at 1 kHz and 15.7 for a resonance frequency at 10 kHz on a bubble of CO_2 at the depth of 120 m, based on Devin's theory (Devin, 1959) and following the procedure in Leighton (1994). The predicted bandwidth of the bubbles from the calculated quality-factor is 54 Hz for 1 kHz and 640 Hz for 10 kHz. However, percentage differences between the measured quality-factor and the calculated quality-factor was investigated to 3.5–40% (Walton et al., 2005). Therefore, using the calculated lower bandwidth limit 54 Hz as a reference value, we investigate the bandwidth threshold $\mathrm{Th}_{\mathrm{band}}$ in Section 6.2.

Setting low thresholds will increase the probability of false alarming, i.e. noise pulses are identified as bubbles, whereas setting high thresholds there will be fewer false alarms, i.e. removing more noise pulses, but may also reduce the probability of detecting a bubble and decrease the number of identified bubbles. A good detector uses a threshold that offers a low false alarm rate and a high probability of detecting a bubble. We will investigate the effect of the thresholds in Section 6.

3.2.2. Bubble radius and gas flux computation

Each patch in the cross-spectrogram is taken to correspond to the sound of an individual bubble formation event. The frequency bin containing most energy, $f_{\max}$, is taken as a measure of the natural frequency of the bubble and we can determine the corresponding radius R_0 [m] of the bubble using the Minnaert's formula (Minnaert, 1933):

$$R_0 = \frac{1}{2\pi f_{\max}} \sqrt{\frac{3\gamma P_{\mathrm{st}}}{\rho_w}}, \tag{13}$$

where γ is the polytropic index of the gas, and ρ_w is the seawater density [kg/m^3]. The P_{st} [Pa] at depth d [m] is computed as (Leifer and Patro, 2002)

$$P_{\mathrm{st}} = P_{\mathrm{atm}} + \rho_{\mathrm{w}} \mathrm{g}\ \mathrm{d} + 2\gamma/r, \tag{14}$$

where P_{atm} is the atmospheric pressure [Pa], and g is the acceleration due to gravity [m/s^2] assuming a single density values for the seawater.

Finally, assuming N_b bubbles are identified in total for a time interval of T, then the gas flux can be calculated by integrating the volume G [L/min] of all bubbles as

$$\mathrm{G} = \frac{1}{T} \sum_{n_b=1}^{N_b} \frac{4}{3} \pi R_{n_b}^3, \tag{15}$$

where R_{n_b} is the radius of the nth identified bubble in a time interval, with which a bubble size distribution can also be concluded.

4. Optical bubble identification

Here we present an optical method for determining the bubble size distribution to complement the acoustic method. The technique subtracts a background image prior to tracking and measuring bubbles present. The optical data is analysed through two steps: a frame by frame image processing algorithm, and a multi-frame tracking algorithm. The frame by frame image processing algorithm takes a single colour image

of bubbles in the water column as well as the background, and converts it to a binary image that shows positions of bubbles.

4.1. Frame by frame image processing

The calculation of bubble size through detection of the bubble wall and inferring volume, as here, is the most popular photography method for inferring a bubble size distribution (BSD), but it is not the only one. Leighton and Walton (1987) demonstrated how stroboscopic illumination of the flow could detect the rise time of many bubbles simultaneously, and from that infer their size if the water were still or its local flow speed know, and bubble-bubble-interactions (if they exist) are corrected for.

The initial step is to calculate a background image by converting a large number of video frames to grey scale, summing the frames and dividing by the number used to determine the average frame. This grey scale background image with no bubbles present is then sharpened and edge detected using the absolute Sobel edge detection (Kittler, 1983) kernel to produce the image subsequently used to remove the background. Once the background is computed the frame by frame process is a sequential series of image processing algorithms: conversion to grey scale, application of the absolute Sobel edge detector (Kittler, 1983), subtraction of the previously calculated background image, application of Gaussian blur, image threshold, and then flood-filling the background to fill any gaps in the bubbles. The result of these steps is the desired binary frame that shows the shape and location of the bubbles within the water column. Next the tracking section of the algorithm uses these binary frames to estimate gas flux and bubble size distribution.

4.2. Multi-frame tracking

The tracking algorithm starts by scanning the bottom of a binary frame for bubbles and if detected their pixel and location information are recorded. In the next frame these identified bubbles are tracked by taking their previous positions and determining a new position based on a prior displacement per frame that is updated as a bubble travels through consecutive frames. To determine new position of these bubbles, coordinates from a Gaussian distribution are sampled. The bubbles are identified and tracked in every frame of the video until each bubble passes above a certain point in the frame. At this point the bubble's estimated average volume and radius is saved and this output is used to produce bubble size distribution and gas flux estimates.

A single scaling factor is used convert all bubble measurements from pixels to cm based on observations of a scale bar at the centre of the seep (28 pixels/cm) prior to recording. We assume that all bubbles remain within a 10 cm radius of this central point (and note that majority are far closer than this). A bubble 10 cm closer to the camera than this point will appear 32% larger than it truly is and a bubble 10 cm further away would appear 25% smaller than it truly is. While this may appear a significant error margin, assuming that the bubbles are equally distributed either side of this central point, with a great enough bubble population this effect is greatly reduced as the relative overestimations and underestimations cancel each other out. Due to the Gaussian blur bubbles smaller than 52 pixels cannot be detected meaning we do not expect to detect bubbles from the seep with an equilibrium radius smaller than 0.07 cm.

4.3. Volume estimate

To estimate the average volume and radius of each bubble the horizontal volume of revolution was calculated for each bubble in each frame. In general the shape of the bubbles as we observed them tended to be more closely resembling flat ellipsoids meaning that the horizontal volume calculation seemed more appropriate. Then the average volume is calculated by averaging over the frames it appears in.

In the normal discrete volume of revolution calculation $\pi|x_i - \bar{x}|\delta x^2$ (where x_i is the horizontal coordinate of the ith pixel, $\bar{x}$ is the mean horizontal coordinate of all the pixels and δx is the height and width of a single pixel) represents half the volume of a ring of radius $|x_i - \bar{x}|$ and cross sectional area δx^2.

As measured from the field, the horizontal coordinate u is not in the correct units as it is in pixel number rather than cm. Thus in order to generate a volume of revolution it must be converted to cm. This means that u must be multiplied by δu (the width and height of a single pixel), which gives $\pi|u_i\delta u - \bar{u}\delta u|\delta u^2$ then simplifies to $\pi|u_i - \bar{u}|\delta u^3$. Therefore, the volume of revolution is calculated from the summation

$$V = \sum_{i=1}^{N} \pi|u_i - \bar{u}|\delta u^3, \tag{16}$$

where u_i is the horizontal coordinate of the ith pixel in the bubble, $\bar{u}$ is the average horizontal coordinate of the pixels within the bubble and δu is the physical length of 1 pixel at the scale of the bubble. The horizontal coordinate u represents the horizontal position of the pixel in number of pixels from the left of the frame. It is essentially the index of the pixel within the array that makes up the frame.

The physical length is normally done by placing an object of known size (such as a board with scale markings on it) in the position of the bubbles in view of the camera. Then we count the length of this known scale in pixels in the video and divide the true length of the object by the number of pixel lengths in the video to obtain an approximate scale factor for the bubbles in the plume. This scale can also be calculated based off of an object at a different distance from the bubbles in the frame and recalculated to the positions of the bubbles using trigonometry.

This comes with the caveat that any bubbles not in the position where the scale measurement was taken will not be calculated to the right size but provided that the seep is roughly stationary then any deviations should cancel each other out. The equivalent radius of each individual bubbles is calculated as being the radius of a sphere that would have an equivalent volume to the bubble in question. This approach suits the shape of the bubbles that were being observed in the video.

5. Experiment

This paper reports the data collected from the STEMM-CCS gas release experiment conducted in the central North Sea in May 2019. This section describes the passive acoustic and optical packages of the experiment with the design and deployment of an array of five hydrophone elements and an optical frame.

5.1. Controlled gas-release STEMM-CCS experiment in the North Sea

The central North Sea has been identified as a potential CCS site (Strachan et al., 2011; Shell, 2017). The STEMM-CCS CO_2 injection site was situated 1000 m south-east of the Goldeneye platform (Flohr et al., 2020b), around 100 km east of Scotland (Fig. 1) at 120 m water depth. We conducted a controlled sub-seabed CO_2 release experiment to replicate a realistic leakage scenario to test the applicability of a variety of leakage monitoring techniques. CO_2 gas was injected into the unconsolidated sediments 4 m beneath the seabed over a 5-week period, during which the flow rate was increased from 0 to 143 kg/day (50 L/min STP) (Flohr et al., 2020b). The temporal and spatial behaviour of gas seeps originating from the gas injection site (Fig. 1) was monitored using an array of hydrophones.

Eight seeps with moderate and relatively high flow rates (Flohr et al., 2020a) were visually observed (Fig. 1) and acoustically recorded by hydrophone array (Fig. 2(a)) in response to a known gas injection flow rate 143 kg/day (Fig. 1). The CO_2 bubbles seeping from the seep 6 were optically recorded by a high-quality underwater video equipment

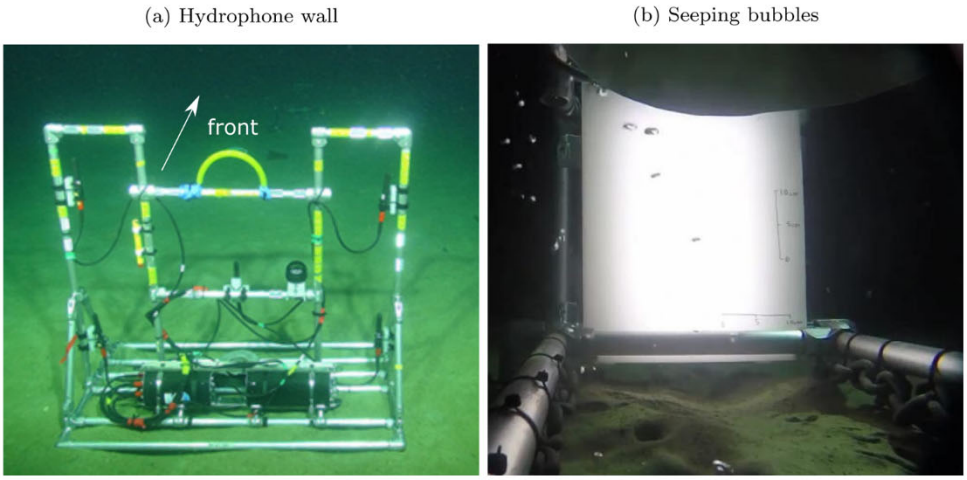

Fig. 2. Photographs showing (a) the hydrophone wall deployed on the seabed using an ROV; (b) CO_2 bubbles escaping from the seep 6 (position shown in Fig. 1), recorded by a camera fixed on a frame.

(SONY FDR-X3000 Action Camera, with UltraHD resolution 720p at 30fps) fixed on a frame with a white board as the background shown in Fig. 2(b). In general, the migration pathways of injected gas can be complex within the subsurface sediment layers (Roche et al., 2020). Furthermore, they can be influenced by numerous chemical/biological/physical factors. Consequently, it is possible for seeps to release gas into the water column intermittently or as time-varying flux in response to a known and relatively stable gas injection flow rate into the sediment. The hydrophone wall was positioned using a remotely operated underwater vehicle (ROV) at a distance of 3.3 m east from the central point directly above the end of the gas diffuser (Fig. 1).

The data used here were collected when the gas injection flow rate was 143 kg/day between Greenwich Mean Time (GMT) 16:30 on 21st May 2019 and 04:30 on 22nd May 2019, during which time the research ship was stationed at a distance of 1 km from the experimental site. The seabed sediment types at the experiment location were mainly sand and mud as shown in Fig. 2(b), and the temperature of the North Sea bottom water was 7.7 °C. Visual observation of the eight small seeps showed that each seep hole had a radius between 1 cm and 10 cm.

5.2. Hydrophone array deployment

Fig. 3(a) shows the schematic drawing of the hydrophone wall. The five hydrophones (Geospectrum M36) were linked to the acoustic recorder (RS-ORCA), which was used to archive the sound of bubbles emerging from the seabed. This setup constitutes an hydrophone array as shown in Fig. 2(a) while a full diagram of the design is shown in Fig. 3. These hydrophone measurements were calibrated using manufacturer supplied receive sensitivity (−164.5 dB re 1 V/μPa) over frequency range 30 Hz to 48 kHz with variation of ±3 dB. A gain of 15 dB was applied to each of the recording channels, and a sampling frequency of 96 kHz was used. The RS-ORCA recorder and hydrophones were operated by internal and external batteries, supporting long-term deployments. The hydrophones were programmed to record data at predetermined time intervals of 5 min on and 5 min off.

5.3. Optical frame deployment

The optical frame (Fig. 3(b)) was positioned over seep 6 (see Fig. 1) using an ROV so that the CO_2 bubbles emerged between the camera and the illuminated whiteboard. The distance between the camera and the whiteboard was 1 m.

6. Results and discussion

In this section, we apply the proposed techniques to the experimental acoustic data to identify single bubbles from background noise, and investigate threshold criteria for the determination of bubble size distribution and gas flux. We also investigate the influence of tidal activity on ebullition, as previous studies have demonstrated an inverse correlation (Blackford et al., 2014, 2015; Bergès et al., 2015).

6.1. Identification of single bubble

Fig. 4 shows the spectrogram and cross-spectrogram for four seconds of data recorded on 21st May, 2019. It is difficult to identify any bubbles from the spectrogram of this data recorded from a single hydrophone (Fig. 4(a)) as a consequence of the high level background noise. While it is easier to identify a few bubbles from the cross-spectrogram (Fig. 4(b)), as the noise level is reduced by the use of the cross-spectrogram. Normalising the spectrogram and cross-spectrograms (12) makes the bubble signals more apparent (Fig. 4(c) and (d)), in these frames we only show the positive values for the two representations. Fig. 4(e) and (f) highlights the effect of thresholding on cross-spectrogram with 15 dB and 25 dB energy thresholds applied. Energy thresholding improves bubble identification, and the frequency of bubble generated acoustic waves largely in the interval 1 kHz (1.2 cm radius bubbles at 120 m) to 11 kHz (0.09 cm radius bubbles at 120 m). Increasing the threshold suppresses noise much more than bubble sound, particularly for sound from small and quiet bubbles which is frequency-dependent. There are still some noise pulses which can be identified with the threshold $Th_{eng} = 15$ dB, this can be further reduced by adjusting the bandwidth threshold. The sounds are transients with finite bandwidth, which can be up to 1.5 kHz as shown in Fig. 4(e) and (f). The bandwidth of bubbles sounds is wider than individual peaks present within ambient noise (Fig. 8). Fig. 4(g) and (h) shows the identified "bubbles" with different bandwidth thresholds $Th_{band} = 0$ Hz and 100 Hz. We can see that some identified "bubbles" at $Th_{band} = 0$ Hz with small bandwidth are not identified by using $Th_{band} = 100$ Hz. To choose appropriate thresholds, we need to investigate the distribution for all pulses.

6.2. Detection threshold investigation

This subsection evaluates the selection criteria of two detection thresholds used. Fig. 5 shows the energy distribution (i.e., normalised cross-spectrogram energy distribution) of "bubbles" identified in a 90 s section of data at various energy and frequency bandwidth thresholds. Fig. 5 highlights that the shape of the distribution is insensitive to the

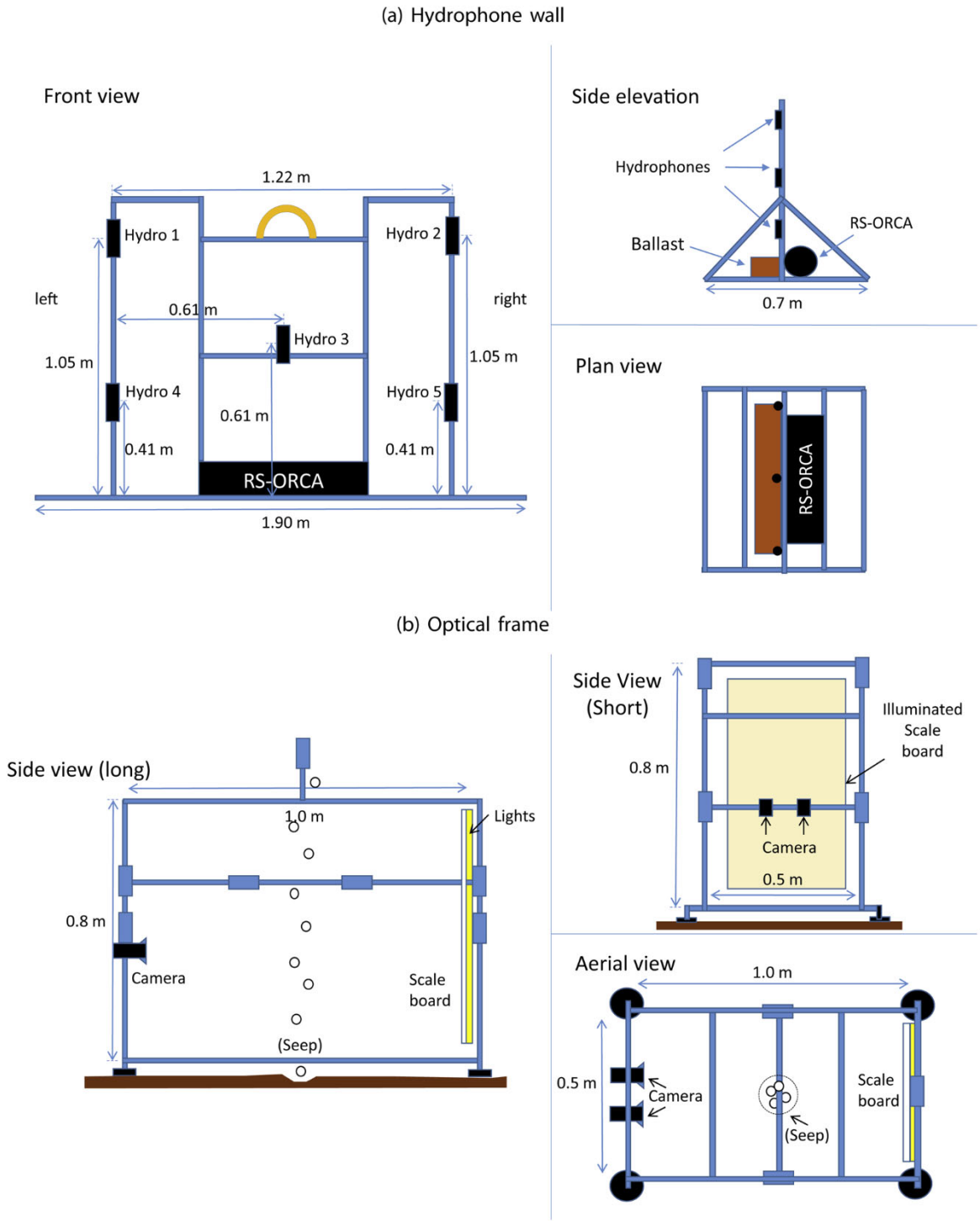

Fig. 3. Plans of the acoustic and optical landers used to determine bubble size distributions. (a) The hydrophone wall, comprising five hydrophones and an acoustic recorder (*RS-ORCA*); the positions of them are shown. See *in situ* photograph in Fig. 2(a); (b) the optical frame, comprising video camera and whiteboard; the positions of them are shown. See *in situ* photograph in Fig. 2(b).

choice of energy threshold (10 dB or 15 dB), whereas it is sensitive to the choice of bandwidth threshold. Increasing the bandwidth threshold restricts the detection of low bandwidth signals which is more about noise impulses.

Fig. 6 shows the frequency bandwidth distribution of "bubbles" identified in the same 90 s section of data at various energy thresholds. Fig. 6 highlights that more than 60% of the frequency bandwidths of the measured sounds are in the interval of [0, 160] Hz. Within this interval, two peak bars can be observed, which are the 2nd bar at bandwidth [30, 50] Hz and the 4th bar at bandwidth [90, 110] Hz. At the thresholds of 5 dB and 10 dB the 2nd bar is higher than the 4th bar; while at the thresholds of 15–20 dB the 2nd bar is lower than the 4th bar. This indicates that the dominant contributor of the measured sound changes (from background noise to bubble sound) from the threshold 10 dB to 15 dB. Further, the arrows in the interval [0, 160] dB reveal a trend change of the bandwidth distribution from the threshold 10 dB to 15 dB.

Fig. 7 shows example waveforms that have been band-pass filtered at various frequencies ranging from 1 kHz to 10 kHz. Note that the

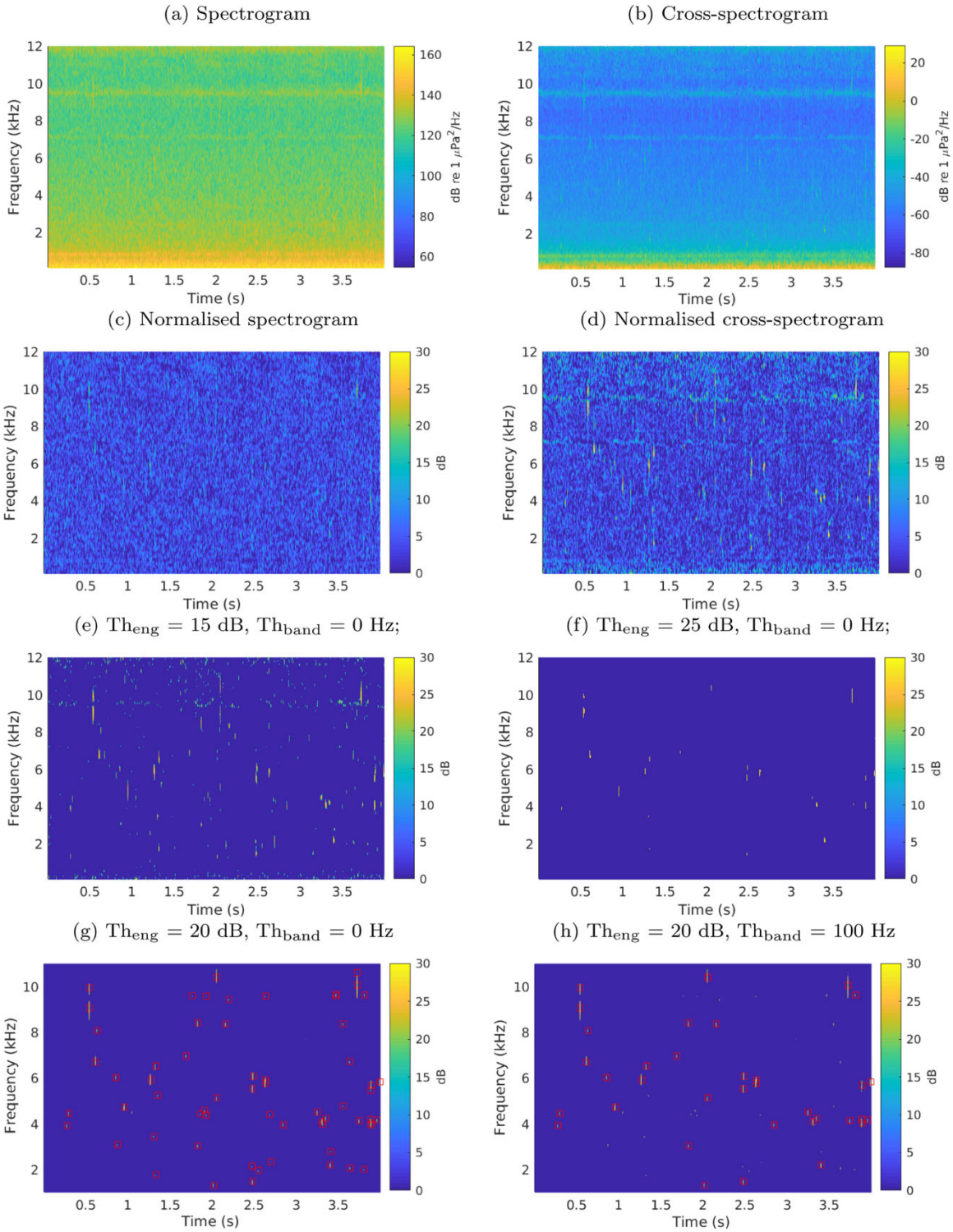

Fig. 4. Spectrogram and cross-spectrogram using short-time Fourier transforms; only positive values are shown. (a) Spectrogram of data from hydrophone 1; (b) cross-spectrogram of data from 5 hydrophones; (c) normalised spectrogram; (d) normalised cross-spectrogram; (e) $Th_{eng} = 15$ dB, $Th_{band} = 0$ Hz; (f) $Th_{eng} = 25$ dB, $Th_{band} = 0$ Hz, from which bubbles are clearly shown as yellow dots dominantly at frequency interval 1–11 kHz; (g) identified "bubbles" are shown in red rectangles with $Th_{eng} = 20$ dB and $Th_{band} = 0$ Hz; (h) defining $Th_{eng} = 20$ dB, $Th_{band} = 100$ Hz, single bubbles are easily identified from the cross-spectrogram as compared to the spectrogram analysis using single hydrophone. As shown in Fig. 8, the frequency bandwidths of bubble sounds are wider compared to ambient noise.

frequency shown here is the frequency where a bubble shows the highest energy in cross-spectrogram. This figure is obtained by performing a cross-spectrum analyses first (including 5 hydrophones) to determine bubble frequency ranges and then applying a band-pass filtering on identified bubble signals (15 ms) received by hydrophone 4.

Based on the cross-spectrogram, the energy thresholds are investigated from 5 dB to 30 dB, and the frequency bandwidth thresholds are investigated from 30 Hz to 70 Hz. This investigated interval covers the calculated lower bandwidth limit (54 Hz) from the quality-factor at 1 kHz (see Section 3.2.1). Robust detection thresholds can be determined in comparison

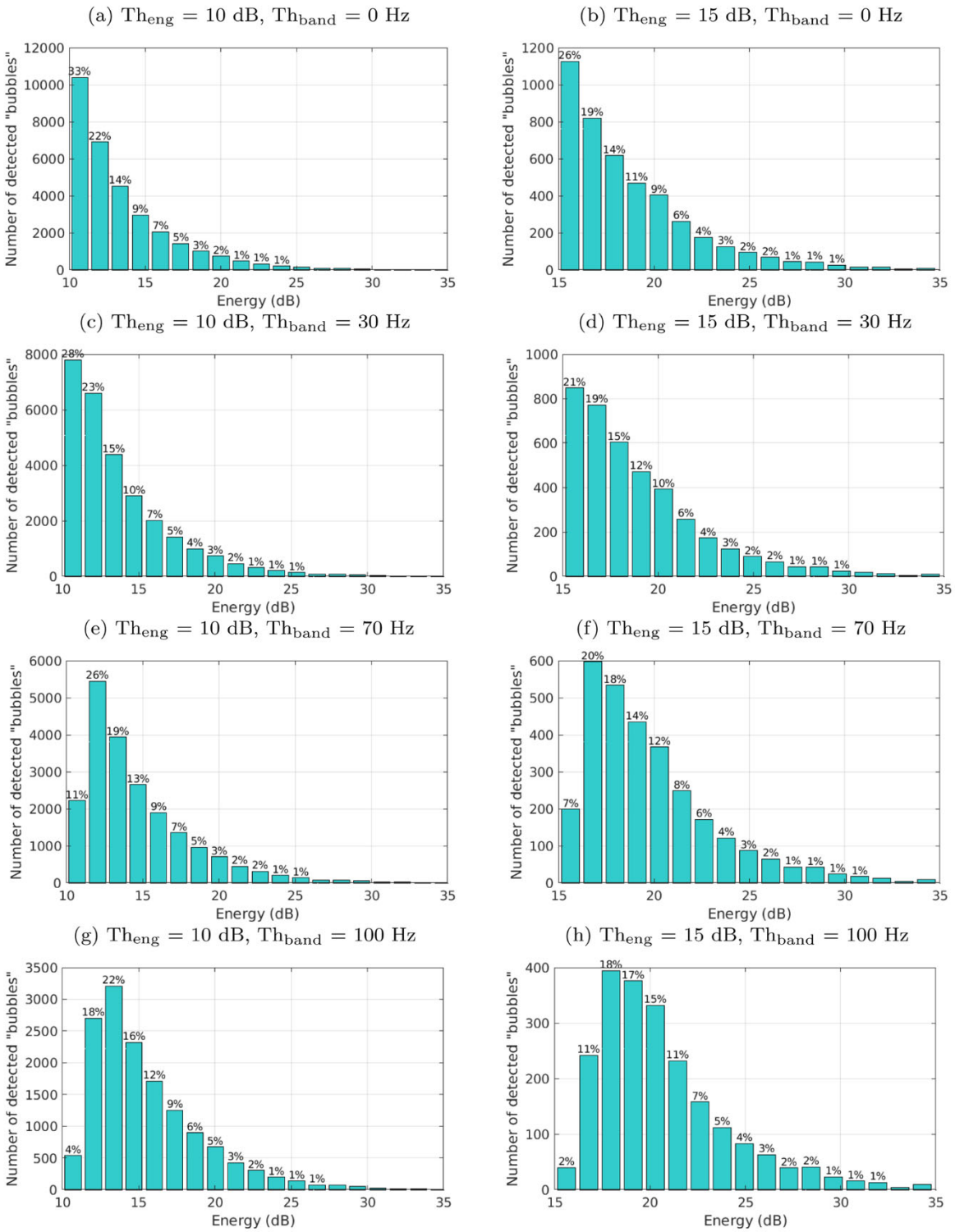

Fig. 5. Energy distribution of detected "bubbles" at various energy and frequency bandwidth thresholds with 90 s data as an example; the % value on top of each bar shows the percentage of bubble number for each energy unit. (a) $Th_{eng} = 10$ dB, $Th_{band} = 0$ Hz; (b) $Th_{eng} = 15$ dB, $Th_{band} = 0$ Hz; (c) $Th_{eng} = 10$ dB, $Th_{band} = 30$ Hz; (d) $Th_{eng} = 15$ dB, $Th_{band} = 30$ Hz; (e) $Th_{eng} = 10$ dB, $Th_{band} = 70$ Hz; (f) $Th_{eng} = 15$ dB, $Th_{band} = 70$ Hz; (g) $Th_{eng} = 10$ dB, $Th_{band} = 100$ Hz; (h) $Th_{eng} = 15$ dB, $Th_{band} = 100$ Hz. Impulse noises dominantly possess low energy and bubbles possess relatively high energy. The distribution shapes are similar at the same Th_{band} for different Th_{eng}, while the energy of dominant identified "bubbles" increases as Th_{band} increases.

to ambient noise recorded prior to gas injection. We compare the acoustic data recorded at maximum flow rates of 143 kg/day (50 L/min STP) with that recorded prior to injection on 9th May 2019. Fig. 8 (a) shows the number of identified "bubbles" for different frequency bandwidth thresholds, as a function of the energy threshold Th_{eng}. The curves for different bandwidth thresholds broadly have the same shape. The number of "bubbles" is identified to about 100 in 5 min at the energy threshold of 14 dB with the background data, revealing a negligible number of false detections with this choice of threshold. This provides a threshold with low level background noise for quantifying the gas flux. The number of

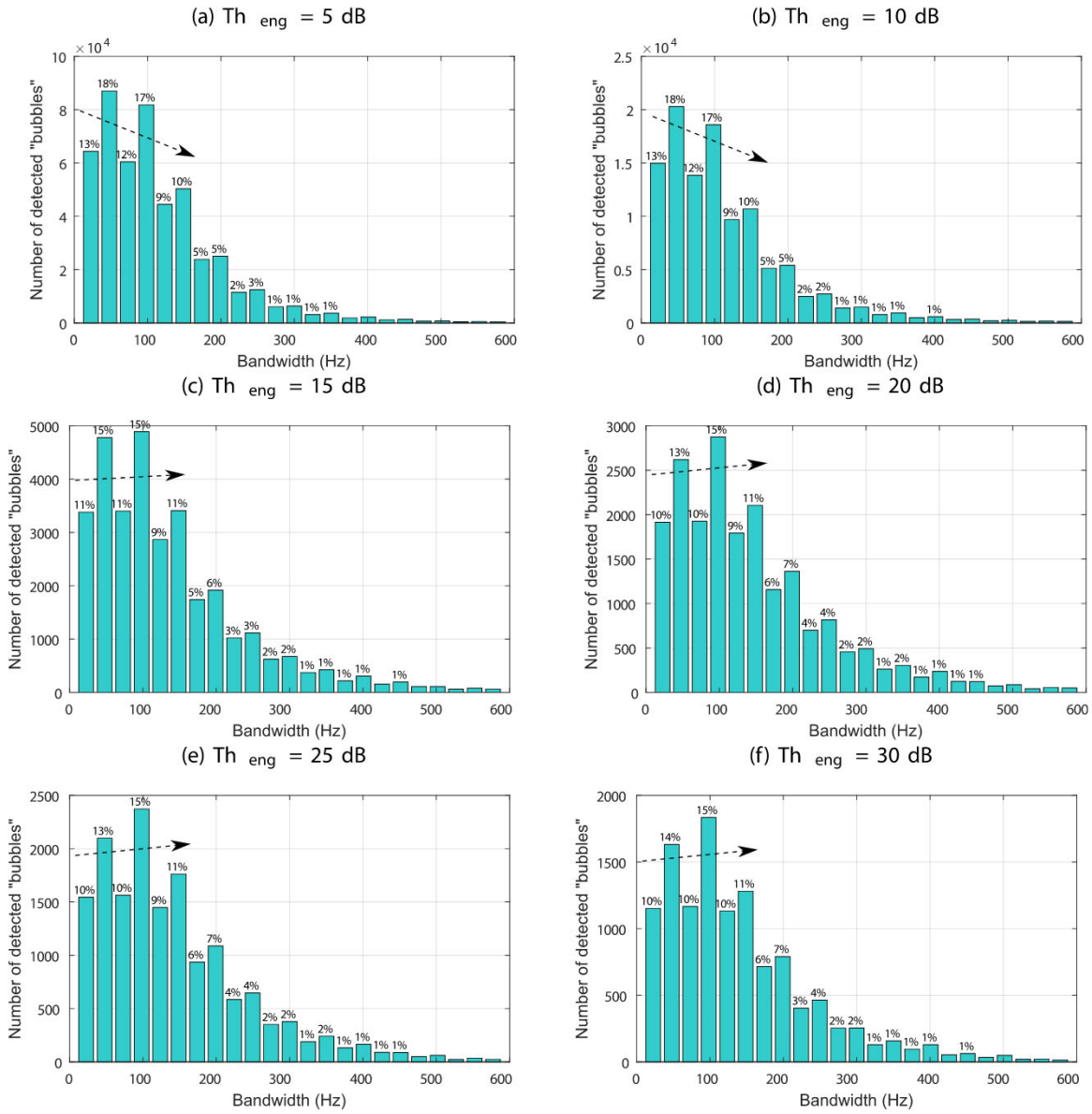

Fig. 6. Frequency bandwidth distribution of detected "bubbles" at various energy thresholds with 90 s data as an example where $Th_{band} = 0$ Hz; the % value on top of each bar shows the percentage of bubble number for each bandwidth unit. (a) $Th_{eng} = 5$ dB; (b) $Th_{eng} = 10$ dB; (c) $Th_{eng} = 15$ dB; (d) $Th_{eng} = 20$ dB; (e) $Th_{eng} = 25$ dB; (f) $Th_{eng} = 30$ dB. In the dominant bandwidth interval [0, 160] Hz, two substantial peak bars are observed, which are classified from two different impulse noises, here the background noise ([30, 50] Hz) and the bubble sound ([90, 110] Hz). The arrow on each figure shows the distribution difference in this bandwidth interval ([0, 160] Hz) at thresholds 5–10 dB and thresholds 15–30 dB, indicating a dominant noise transition between thresholds 10 dB and 15 dB.

bubbles on "gas curves" changes from fast to slow in the energy threshold interval between 13 and 15 dB.

Fig. 8(b) shows the average bandwidth (see Fig. 6 for bandwidth distribution at threshold $Th_{band} = 0$ Hz) above the threshold, which highlights that these 143 kg/day (50 L/min STP) gas curves reach the highest level and tends to be stable starting from 13 dB at all bandwidth thresholds, revealing that gas bubbles dominate acoustic pulses at this threshold. This provides a lower energy threshold for quantifying the gas flux. With an increase of 40 Hz in the frequency bandwidth threshold from 30 Hz to 70 Hz, the average bandwidth changes 20–30 dB across all the energy thresholds, resulting in a Gaussian-like distribution of the frequency bandwidth of the bubble acoustic waves. We select the frequency threshold (30–70 Hz) to be smaller than half of the highest value 160–180 Hz at 143 kg/day, and larger than half of the highest value 115 Hz at 0 kg/day. Fig. 8(c) shows the average energy where the rise of all the gas curves changes from fast to slow at the energy threshold interval 13–15 dB, which shows the domination of gas bubbles. Furthermore, the average energy difference between 143 kg/day and the ambient sounds, when no injection was occurring, increases significantly after the threshold of 13 dB, which indicates more bubbles and less noises. This identified average energy provides a lower threshold.

Based on this threshold investigation, we obtain that the gas flux for a 5 min data block is equivalent to 32–88 kg/day (0.9–2.5 L/min at seabed or 11–30 L/min STP) (Fig. 8(d)), with an average value of 60 kg/d (1.7 L/min at seabed) at a tidal height 118.7 m (Fig. 10).

6.3. Determination of bubble size and gas flux

Fig. 9 compares the bubble size distributions based on acoustic and optical measurements. The result for the acoustics is obtained using the energy threshold (Th_{eng}) of 20 dB and the frequency bandwidth threshold (Th_{band}) is set to 100 Hz. The acoustically derived modal bubble radius is 0.17 cm with most bubbles at radii between 0.15 and 0.3 cm (Fig. 9(a)).

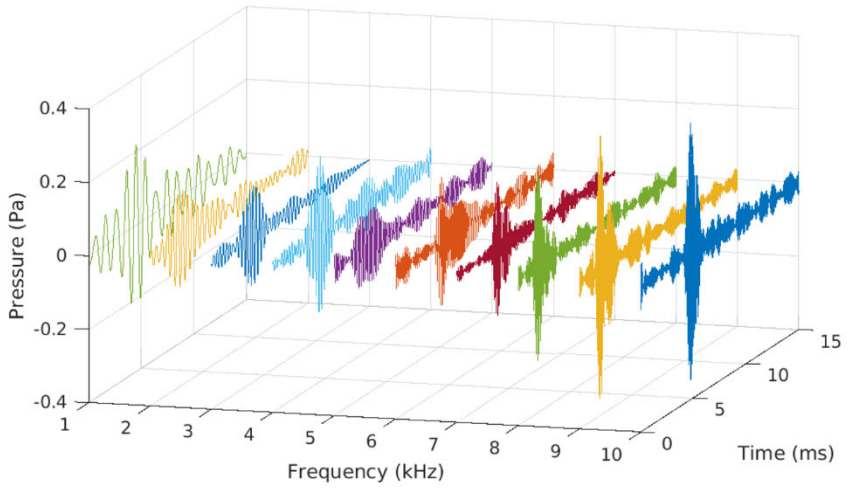

Fig. 7. Band-passed waveforms of identified bubbles recorded by hydrophone 4 at various frequencies from 1 kHz to 10 kHz. The duration of bubble generated signals can extend up to 15 ms with majority of peaks observed around 5 ms.

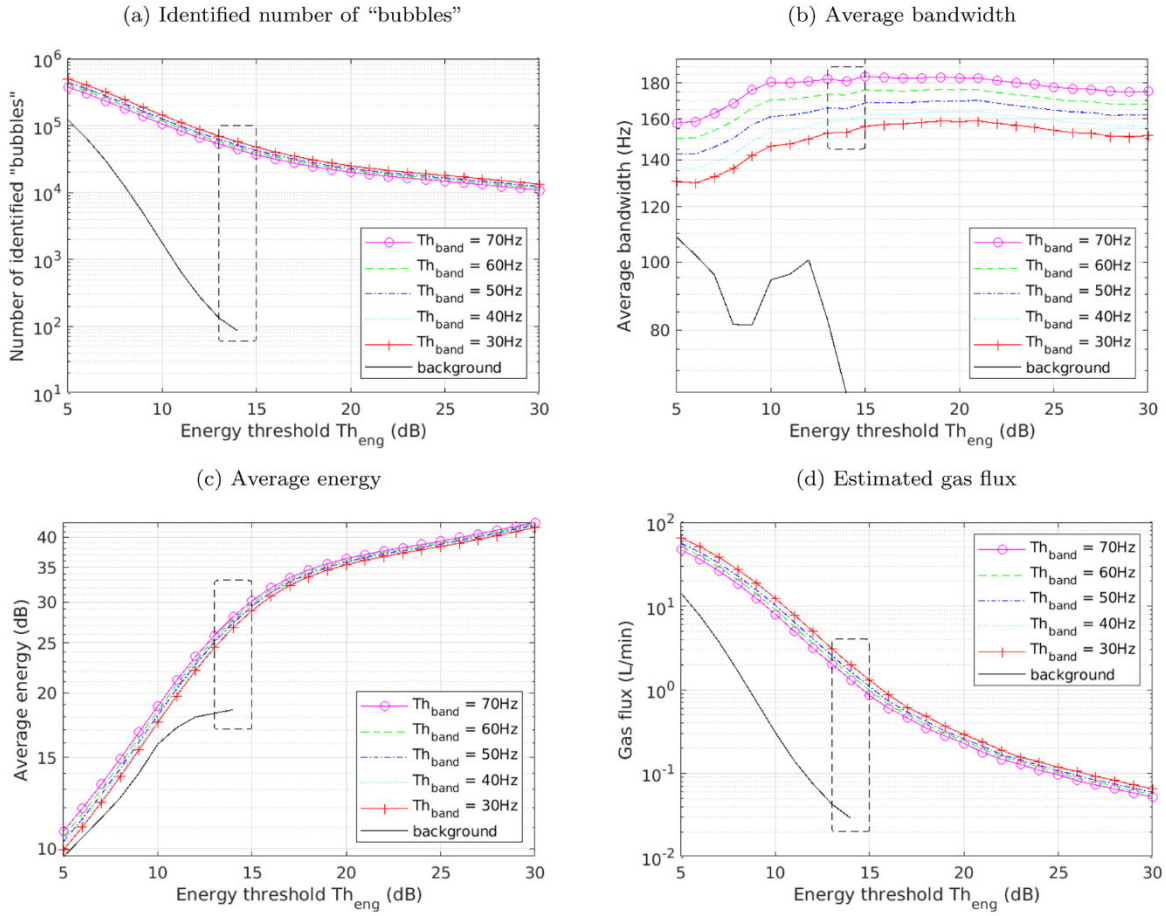

Fig. 8. Investigation of the effect of the thresholds, Th_{eng} and Th_{band}, based on two 5 min records, collected on 21st May 2019 (143 kg/day gas injection rate) and 9th May 2019 (0 kg/day injection rate, i.e. only background noise is measured). (a) The number of bubbles detected; from the background data (solid line) it can be seen that the choice of $Th_{eng} = 15$ dB corresponds to 100 bubbles being identified, presumably falsely, which is <1% of the number of bubbles detected on the 21st. (b) Average bandwidth of the bubbles detected for each choice of threshold (see Fig. 6 for bandwidth distribution). For larger choices of Th_{band} the average bandwidth of bubbles detected at an energy threshold greater than 10 dB is reasonably constant, suggesting that the detect events have a consistent bandwidth. (c) Average energy of the bubbles detected with the different threshold choices; the background noise curve is approximately parallel to that of the data collected during the release, up to threshold of around 13 dB. This suggests that below 13 dB the detections are predominantly false alarms. (d) Estimated gas flux; from the identified threshold interval, the gas flux is estimated to 32–88 kg/day (0.9–2.5 L/min at seabed), with an average of 60 kg/day (1.7 L/min at seabed). Dashed rectangles show 13–15 dB horizontally on these curves. We only present 'background noise' curve up to $Th_{eng} = 14$ dB, as the number of identified "bubbles" is too small (less than 100) which does not hold statistical property.

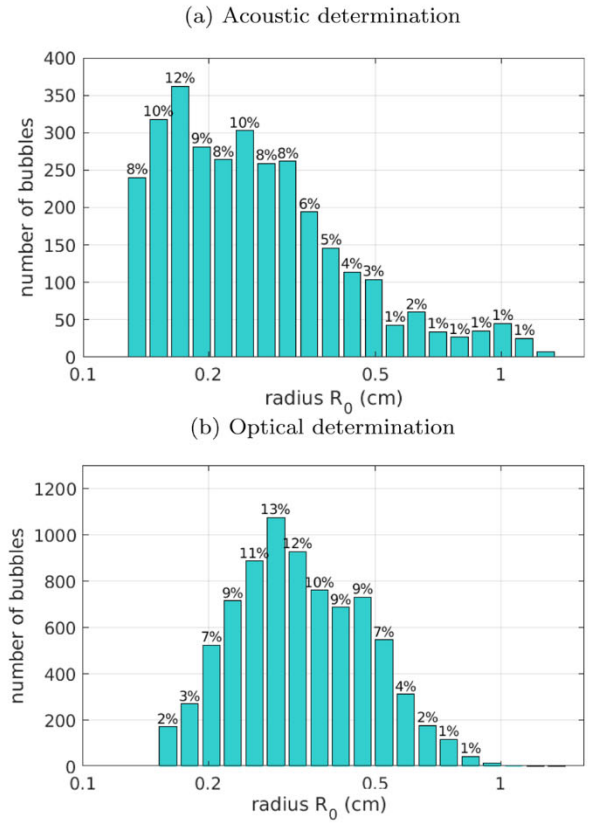

Fig. 9. Determined bubble size distribution; the % value on top of each bar shows the percentage of bubble number for each radius unit. (a) passive acoustics; the modal bubble radius is 0.17 cm, thresholds of $Th_{eng} = 20$ dB and $Th_{band} = 100$ Hz were used. (b) optical methods applied to seep 6 (Fig. 1); the modal bubbles radius is 0.3 cm. The optical method is not sensitive to small bubbles (radii less than 0.2 cm) and underestimates their abundance.

The optical measurements were focussed on seep site 6 (Fig. 1) and analysis of the data shows most bubbles occurring at radii between 0.2 and 0.5 cm, with a modal value of 0.3 cm (Fig. 9(b)). The optical measurements are only for one seep, and small bubbles less than 0.2 cm were not reliably identified. This is because the optical determination is based on the optical scattering strength from bubbles, which is unable to detect most of the small bubbles due to strong optical penetration and attenuation as well as weak optical scattering of small bubbles. The optical method in the present study computes the bubble size distribution from a single seep for a short period of time. To compute the total flux, we assume all seeps emit bubbles with the same distribution and multiply by the number of seeps. Whereas the acoustic method provides long-term monitoring of all seeps. The optically estimated gas flux focusing on the single seep 6 is 8.2–13.0 kg/day (0.24–0.38 L/min at seabed).

Fig. 10 shows variation of the acoustically estimated gas flux with tidal height for a period when background noise was a minimum. A broad negative correlation is observed where gas flux decreases as tidal height increases, with a Pearson cross-correlation coefficient (Benesty et al., 2009) of −0.41. This negative correlation is due higher hydrostatic pressure during high tide suppressing gas emissions from the seabed.

7. Conclusions and discussion

In this paper, we developed and applied an adaptive acoustic single bubble identification technique, and compared it to an optical bubble identification method, using data collected during a controlled CO_2 release experiment (STEMM-CCS) in the central North Sea. The hydrophone array recorded signals from eight ebullition sites at the seabed,

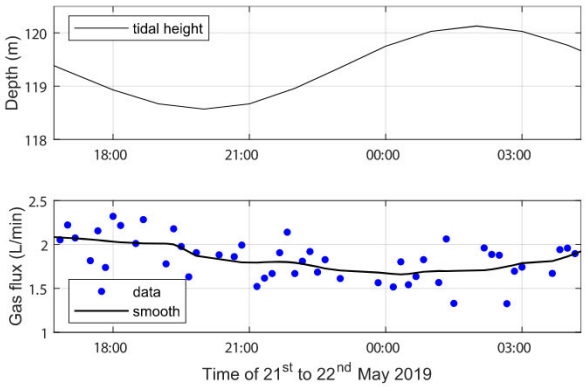

Fig. 10. Variation of acoustically quantified gas fluxes with tidal height for a period when background noise was a minimum. There is a broad inverse correlation between gas flux and tidal height (Pearson cross-correlation coefficient of −0.41). The thresholds for quantifying the gas flux are $Th_{eng} = 14$ dB and $Th_{band} = 50$ Hz.

while the optical data was collected at a single seep site. The acoustic technique incorporates bubble acoustic characteristics from the time-domain and frequency domain, and pulsation strength. It is capable of identifying single bubbles in noisy environments and determining bubble size distribution and gas flux.

At 120 m water depth, the acoustically determined modal bubble radius is 0.17 cm, while the optically determined modal gas radius is 0.3 cm. The optical method under measures smaller bubbles, which is why the modal gas radius is biased higher. Our acoustically determined gas flux across the seabed is 32–88 kg/day for a gas injection rate of 143 kg/day, meaning 22–62% of the CO_2 emerges from the seabed in gaseous form.

The proposed single bubble identification technique is adaptive and can be performed automatically for any length of acoustic signals. This allows long-term underwater acoustic detection and quantification of gas leakage over marine carbon storage reservoirs across the world-wide ocean sub-seabed. This technique is applicable when bubbles are generated as a single stream or multiple streams. However, when the bubbles are generated as groups or plume rather than single stream, it is difficult for the technique to identify single bubbles, which may make the estimate results inaccurate and an alternative way would be the acoustic inversion method (Leighton and White, 2011).

In practice, at carbon capture and storage sites, gas will be injected at much greater depth than that described in this paper. In the unlikely event of gas escaping, gas would be expected to seep over a much wider area of the seabed than that investigated at the STEMM-CCS experimental site. In terms of acoustic monitoring, active acoustic monitoring using ship or AUV-mounted multibeam bathymetry or other sonar systems would be used first to detect any seepage site. Subsequently, the passive acoustic monitoring techniques described here, would be deployed for longer term monitoring, and quantification of any emissions through the seabed.

Author contributions

Jianghui Li: Conceptualization, methodology, software, writing – original draft preparation. Paul R. White: Data curation, methodology, reviewing and editing. Ben Roche: Data curation. Jonathan M. Bull: Data curation, supervision, reviewing and editing. Timothy G. Leighton: Reviewing and editing. John W. Davis: Data curation. Joseph W. Fone: Methodology.

Conflict of interest

The authors declare that there is no conflict of interest.

Declaration of Competing Interest

The authors report no declarations of interest.

Acknowledgements

Funding was provided by the European Union's Horizon 2020 Research and Innovation Programme under the grant agreement number 654462 (STEMM-CCS). We are grateful to the Captain of the RRS 'James Cook' and crew for enabling the scientific measurements at sea during the JC180 cruise.

Appendix A. Single bubble identification algorithm

Algorithm 1 details the algorithm for single bubble identification.

Algorithm 1. Single bubble identification

Require: $\mathrm{Th}_{\mathrm{eng}}$, $\mathrm{Th}_{\mathrm{band}}$, $\widehat{C}(p,f(b))$
procedure
  for $p = 2 : P-1$ **do** segments
  if $\widehat{C}(p,f(b)) < \mathrm{Th}_{\mathrm{eng}}$ ▷ energy threshold **then**
    $\widehat{C}(p,f(b)) = 0$;
  end if
  for $b = 1 : B$ **do**
    if $\widehat{C}(p,f(b)) > \widehat{C}(p-1,f(b))$ & $\widehat{C}(p,f(b)) > \widehat{C}(p+1,f(b))$ **then**
  save $[p,f(b)]$; ▷ save location of pulses for further process
    end if
  end for
    end for
    Nb $= 0$; ▷ initialize bubble number
    find repeated elements Q for the pth segment ▷ multiple bubbles may be at one segment
    for $q = Q(1) : Q(\mathrm{end})$ **do**
  if $q = Q(1)$ **then**
    $Q_{\mathrm{start}} = q$; ▷ initial frequency for a bubble bandwidth
  else if $q < Q(\mathrm{end})$ **then**
    if $f(q) < f(q+1) - 1$ **then**
  $Q_{\mathrm{end}} = q$; ▷ the end frequency for a bubble bandwidth
  if $f(Q_{\mathrm{end}}) - f(Q_{\mathrm{start}}) >= \mathrm{Th}_{\mathrm{band}}$ ▷ bandwidth threshold **then**
    save Q_{start}, Q_{end}, maximum $\widehat{C}(p,f(Q_{\mathrm{start}} : f(Q_{\mathrm{end}})))$; ▷ identified "bubble"
    Nb $=$ Nb $+ 1$;
    $Q_{\mathrm{start}} = q + 1$;
  else
    $Q_{\mathrm{start}} = q + 1$;
  end if
    end if
  else if $q = Q(\mathrm{end})$ ▷ final frequency for bubble at the pth segment **then**
    $Q_{\mathrm{end}} = c$;
    if $f(Q_{\mathrm{end}}) - f(Q_{\mathrm{start}}) >= \mathrm{Th}_{\mathrm{band}}$ ▷ bandwidth threshold **then**
  save Q_{start}, Q_{end}, maximum $\widehat{C}(p,f(Q_{\mathrm{start}} : f(Q_{\mathrm{end}})))$; ▷ identified "bubble"
  Nb $=$ Nb $+ 1$;
    end if
  end if
    end for
end procedure

References

Atamanchuk, D., Tengberg, A., Aleynik, D., Fietzek, P., Shitashima, K., Lichtschlag, A., Hall, P.O., Stahl, H., 2015. Detection of CO_2 leakage from a simulated sub-seabed storage site using three different types of pCO_2 sensors. Int. J. Greenh. Gas Control 38, 121–134. https://doi.org/10.1016/j.ijggc.2014.10.021.

Bendat, J.S., Piersol, A.G., 2011. Random Data: Analysis and Measurement Procedures, vol. 729. John Wiley & Sons.

Benesty, J., Chen, J., Huang, Y., Cohen, I., 2009. Pearson correlation coefficient. Noise Reduction in Speech Processing. Springer, pp. 1–4.

Bergès, B.J., Leighton, T.G., White, P.R., 2015. Passive acoustic quantification of gas fluxes during controlled gas release experiments. Int. J. Greenh. Gas Control 38, 64–79. https://doi.org/10.1016/j.ijggc.2015.02.008.

Blackford, J., Bull, J.M., Cevatoglu, M., Connelly, D., Hauton, C., James, R.H., Lichtschlag, A., Stahl, H., Widdicombe, S., Wright, I.C., 2015. Marine baseline and monitoring strategies for carbon dioxide capture and storage (CCS). Int. J. Greenh. Gas Control 38, 221–229. https://doi.org/10.1016/j.ijggc.2014.10.004.

Blackford, J., Stahl, H., Bull, J.M., Bergès, B.J., Cevatoglu, M., Lichtschlag, A., Connelly, D., James, R.H., Kita, J., Long, D., et al., 2014. Detection and impacts of leakage from sub-seafloor deep geological carbon dioxide storage. Nat. Clim. Change 4, 1011–1016. https://doi.org/10.1038/nclimate2381.

Caserini, S., Dolci, G., Azzellino, A., Lanfredi, C., Rigamonti, L., Barreto, B., Grosso, M., 2017. Evaluation of a new technology for carbon dioxide submarine storage in glass capsules. Int. J. Greenh. Gas Control 60, 140–155. https://doi.org/10.1016/j.ijggc.2017.03.007.

Cevatoglu, M., Bull, J.M., Vardy, M.E., Gernon, T.M., Wright, I.C., Long, D., 2015. Gas migration pathways, controlling mechanisms and changes in sediment acoustic properties observed in a controlled sub-seabed CO_2 release experiment. Int. J. Greenh. Gas Control 38, 26–43. https://doi.org/10.1016/j.ijggc.2015.03.005.

von Deimling, J.S., Greinert, J., Chapman, N., Rabbel, W., Linke, P., 2010. Acoustic imaging of natural gas seepage in the north sea: sensing bubbles controlled by variable currents. Limnol. Oceanogr.: Methods 8, 155–171. https://doi.org/10.4319/lom.2010.8.155.

von Deimling, J.S., Rehder, G., Greinert, J., McGinnnis, D., Boetius, A., Linke, P., 2011. Quantification of seep-related methane gas emissions at Tommeliten, North Sea. Cont. Shelf Res. 31, 867–878. https://doi.org/10.1016/j.csr.2011.02.012.

Devin Jr., C., 1959. Survey of thermal, radiation, and viscous damping of pulsating air bubbles in water. J. Acoust. Soc. Am. 31, 1654–1667. https://doi.org/10.1121/1.1907675.

Dziak, R., Matsumoto, H., Embley, R., Merle, S., Lau, T.K., Baumberger, T., Hammond, S., Raineault, N., 2018. Passive acoustic records of seafloor methane bubble streams on the Oregon continental margin. Deep Sea Res. Part II: Top. Stud. Oceanogr. 150, 210–217. https://doi.org/10.1016/j.dsr2.2018.04.001.

Flohr, A., Matter, J., James, R., Lichtschlag, A., Peel, K., Pearce, C., Connelly, D., 2020a. Quantification of leakage from sub-seabed CO_2 storage using natural and added geochemical tracers. Int. J. Greenh. Gas Control (to be presented).

Flohr, A., Schaap, A., Achterberg, E., Alendal, G., Arundell, M., Berndt, C., Blackford, J., Böttner, C., Borisov, S., Brown, R., Bull, J.M., Carter, L., Chen, B., Dale, A., Beer, D., Dean, d., Deusner, M., Dewar, C., Durden, M., Elsen, J., Esposito, S., Faggetter, M., Fischer, M., Gana, J., Gros, A., Haeckel, J., Hanz, M., Holtappels, R., Hosking, M., Huvenne, B., James, V., Koopmans, R., Kossel, D., Leighton, E., Li, T.G., Lichtschlag, J., Linke, A., Loucaides, P., Matter, S., Monk, J., Mowlem, S., Oleynik, M., Papadimitriou, A., Paxton, S., Pearce, D., Peel, C., Roche, K., Saleem, B., Sands, U., Saw, C., Schmidt, K., Sommer, M., Strong, S., Triest, J., Walk, J., White, J., Widdicombe, P.R., Wilson, S., Wright, E., Wyatt, H., Connelly, J.D., 2020b. Towards improved monitoring of offshore carbon storage: a real-world field experiment detecting a controlled sub-seafloor CO_2 release. Int. J. Greenh. Gas Control 106, 103237–103248. https://doi.org/10.1016/j.ijggc.2020.103237.

Hammond, J., White, P., 1996. The analysis of non-stationary signals using time-frequency methods. J. Sound Vib. 190, 419–447. https://doi.org/10.1006/jsvi.1996.0072.

Hovland, M., Sommerville, J.H., 1985. Characteristics of two natural gas seepages in the north sea. Mar. Petrol. Geol. 2, 319–326. https://doi.org/10.1016/0264-8172(85)90027-3.

Hvidevold, H.K., Alendal, G., Johannessen, T., Ali, A., 2016. Survey strategies to quantify and optimize detecting probability of a CO_2 seep in a varying marine environment. Environ. Model. Softw. 83, 303–309. https://doi.org/10.1016/j.envsoft.2016.06.006.

Jenkins, C.R., Cook, P.J., Ennis-King, J., Undershultz, J., Boreham, C., Dance, T., de Caritat, P., Etheridge, D.M., Freifeld, B.M., Hortle, A., et al., 2012. Safe storage and effective monitoring of CO_2 in depleted gas fields. Proc. Natl. Acad. Sci. U. S. A. 109, E35–E41. https://doi.org/10.1073/pnas.1107255108.

Johnson, G., Raistrick, M., Mayer, B., Shevalier, M., Taylor, S., Nightingale, M., Hutcheon, I., 2009. The use of stable isotope measurements for monitoring and verification of CO_2 storage. Energy Procedia 1, 2315–2322. https://doi.org/10.1016/j.egypro.2009.01.301.

Kita, J., Stahl, H., Hayashi, M., Green, T., Watanabe, Y., Widdicombe, S., 2015. Benthic megafauna and CO_2 bubble dynamics observed by underwater photography during a controlled sub-seabed release of CO_2. Int. J. Greenh. Gas Control 38, 202–209. https://doi.org/10.1016/j.ijggc.2014.11.012.

Kittler, J., 1983. On the accuracy of the Sobel edge detector. Image Vis. Comput. 1, 37–42. https://doi.org/10.1016/0262-8856(83)90006-9.

Kolster, C., Agada, S., Mac Dowell, N., Krevor, S., 2018. The impact of time-varying CO_2 injection rate on large scale storage in the UK Bunter Sandstone. Int. J. Greenh. Gas Control 68, 77–85. https://doi.org/10.1016/j.ijggc.2017.10.011.

Leblond, I., Scalabrin, C., Berger, L., 2014. Acoustic monitoring of gas emissions from the seafloor. Part I: quantifying the volumetric flow of bubbles. Mar. Geophys. Res. 35, 191–210. https://doi.org/10.1007/s11001-014-9223-y.

Leifer, I., Patro, R.K., 2002. The bubble mechanism for methane transport from the shallow sea bed to the surface: a review and sensitivity study. Cont. Shelf Res. 22, 2409–2428. https://doi.org/10.1016/S0278-4343(02)00065-1.

Leifer, I., Tang, D., 2007. The acoustic signature of marine seep bubbles. J. Acoust. Soc. Am. 121, EL35–EL40. https://doi.org/10.1121/1.2401227.

Leighton, T.G., 1994. The Acoustic Bubble. https://doi.org/10.1017/S0022112094214519. ISBN: 0-12-44190-8.

Leighton, T.G., Walton, A.J., 1987. An experimental study of the sound emitted from gas bubbles in a liquid. Eur. J. Phys. 8, 98–104. https://doi.org/10.1088/0143-0807/8/2/005/meta.

Leighton, T.G., White, P.R., 2011. Quantification of undersea gas leaks from carbon capture and storage facilities, from pipelines and from methane seeps, by their acoustic emissions. Proc. R. Soc. A. https://doi.org/10.1098/rspa.2011.0221.

Li, J., 2017. DOA tracking in time-varying underwater acoustic communication channels. MTS/IEEE OCEANS 2017 – Aberdeen 1–9. https://doi.org/10.1109/OCEANSE.2017.8084563.

Li, J., Liao, L., Zakharov, Y.V., 2016. Space-time cluster combining for UWA communications. OCEANS 2016 – Shanghai, IEEE 1–6. https://doi.org/10.1109/OCEANSAP.2016.7485344.

Li, J., Roche, B., Bull, J.M., White, P.R., Davis, J.W., Deponte, M., Gordini, E., Cotterle, D., 2020. Passive acoustic monitoring of a natural CO_2 seep site – implications for carbon capture and storage. Int. J. Greenh. Gas Control 93, 102899–102908. https://doi.org/10.1016/j.ijggc.2019.102899.

Li, J., White, P.R., Bull, B.R.J.M.W., Leighton, D.J., Deponte, T.G., Gordini, M., Cotterle, E.D., 2019a. Natural seabed gas leakage – variability imposed by tidal cycles. MTS/IEEE OCEANS 2019 – Seattle, U.S. 1–6.

Li, J., White, P.R., Bull, J.M., Leighton, T.G., 2019b. A noise impact assessment model for passive acoustic measurements of seabed gas fluxes. Ocean Eng. 183, 294–304. https://doi.org/10.1016/j.oceaneng.2019.03.046.

Li, J., Zakharov, Y.V., 2018. Efficient use of space-time clustering for underwater acoustic communications. IEEE J. Ocean. Eng. 43, 173–183. https://doi.org/10.1109/JOE.2017.2688558.

Loewen, M., Melville, W., 1991. A model of the sound generated by breaking waves. J. Acoust. Soc. Am. 90, 2075–2080. https://doi.org/10.1121/1.401634.

Mabon, L., Shackley, S., Bower-Bir, N., 2014. Perceptions of sub-seabed carbon dioxide storage in Scotland and implications for policy: a qualitative study. Mar. Policy 45, 9–15. https://doi.org/10.1016/j.marpol.2013.11.011.

Minnaert, M., 1933. On musical air-bubbles and the sounds of running water. Lond. Edinb. Dublin Philos. Mag. J. Sci. 16, 235–248. https://doi.org/10.1080/14786443309462277.

Nikolovska, A., Sahling, H., Bohrmann, G., 2008. Hydroacoustic methodology for detection, localization, and quantification of gas bubbles rising from the seafloor at gas seeps from the eastern Black Sea. Geochem. Geophys. Geosyst. 9, 1–13. https://doi.org/10.1029/2008GC002118.

Pachauri, R.K., Allen, M.R., Barros, V.R., Broome, J., Cramer, W., Christ, R., Church, J.A., Clarke, L., Dahe, Q., Dasgupta, P., et al., 2014. Climate Change 2014: Synthesis Report. Contribution of Working Groups I, II and III to the Fifth Assessment Report of the Intergovernmental Panel on Climate Change. IPCC.

Roberts, J.J., Gilfillan, S.M., Stalker, L., Naylor, M., 2017. Geochemical tracers for monitoring offshore CO_2 stores. Int. J. Greenh. Gas Control 65, 218–234. https://doi.org/10.1016/j.ijggc.2017.07.021.

Roche, B., Bull, J.M., Li, J., Marin-Moreno, H., Leighton, T.G., Falcon-Suarez, I., White, P. R., Provenzano, G., Tholen, M., Lichtschlag, A., Li, J., Faggetter, M., 2020. Time-lapse imaging of CO_2 migration within near-surface sediments during a controlled sub-seabed release experiment. Int. J. Greenh. Gas Control (to be presented).

Roelofse, C., Alves, T.M., Gafeira, J., Kamal'deen, O.O., 2019. An integrated geological and GIS-based method to assess caprock risk in mature basins proposed for carbon capture and storage. Int. J. Greenh. Gas Control 80, 103–122. https://doi.org/10.1016/j.ijggc.2018.11.007.

Rychert, K.M., Weber, T.C., 2020. Tests of acoustic target strength and bubble dissolution models using a synthetic bubble generator. J. Atmos. Ocean. Technol. 37, 129–140. https://doi.org/10.1175/JTECH-D-19-0133.1.

Sarıtaş, H., Çifçi, G., Géli, L., Thomas, Y., Marsset, B., Henry, P., Grall, C., Rochat, A., 2018. Gas occurrence and shallow conduit systems in the Western Sea of Marmara: a review and new acoustic evidence. Geo-Mar. Lett. 38, 385–402. https://doi.org/10.1007/s00367-018-0547-5.

Shell, 2017. Goldeneye Gas Platform, United Kingdom. http://www.offshore-technology.com/projects/goldeneye/.

Shitashima, K., Maeda, Y., Sakamoto, A., 2015. Detection and monitoring of leaked CO_2 through sediment, water column and atmosphere in a sub-seabed CCS experiment. Int. J. Greenh. Gas Control 38, 135–142. https://doi.org/10.1016/j.ijggc.2014.12.011.

Stalker, L., Noble, R., Pejcic, B., Leybourne, M., Hortle, A., Michael, K., Dixon, T., Basava-Reddi, L., 2012. Feasibility of monitoring techniques for substances mobilised by CO_2 storage in geological formations. Energy Procedia 23, 439–448. https://doi.org/10.1016/j.egypro.2012.06.039.

Stork, A.L., Allmark, C., Curtis, A., Kendall, J.M., White, D.J., 2018. Assessing the potential to use repeated ambient noise seismic tomography to detect CO_2 leaks: application to the Aquistore storage site. Int. J. Greenh. Gas Control 71, 20–35. https://doi.org/10.1016/j.ijggc.2018.02.007.

Strachan, N., Hoefnagels, R., Ramírez, A., Van den Broek, M., Fidje, A., Espegren, K., Seljom, P., Blesl, M., Kober, T., Grohnheit, P.E., 2011. CCS in the North Sea region: a comparison on the cost-effectiveness of storing CO_2 in the Utsira formation at regional and national scales. Int. J. Greenh. Gas Control 5, 1517–1532. https://doi.org/10.1016/j.ijggc.2011.08.009.

Taylor, P., Stahl, H., Vardy, M.E., Bull, J.M., Akhurst, M., Hauton, C., James, R.H., Lichtschlag, A., Long, D., Aleynik, D., et al., 2015. A novel sub-seabed CO_2 release experiment informing monitoring and impact assessment for geological carbon storage. Int. J. Greenh. Gas Control 38, 3–17. https://doi.org/10.1016/j.ijggc.2014.09.007.

Van Trees, H.L., 2004. Optimum Array Processing: Part IV of Detection, Estimation, and Modulation Theory. John Wiley & Sons.

Vielstädte, L., Linke, P., Schmidt, M., Sommer, S., Haeckel, M., Braack, M., Wallmann, K., 2019. Footprint and detectability of a well leaking CO_2 in the Central North Sea: implications from a field experiment and numerical modelling. Int. J. Greenh. Gas Control 84, 190–203. https://doi.org/10.1016/j.ijggc.2019.03.012.

Walton, A.J., Gunn, M.G., Reynolds, G.T., 2005. The quality factor of oscillating bubbles as an indication of gas content with particular reference to methane. IEEE J. Ocean. Eng. 30, 924–926. https://doi.org/10.1109/JOE.2004.834171.

Zoback, M.D., Gorelick, S.M., 2012. Earthquake triggering and large-scale geologic storage of carbon dioxide. Proc. Natl. Acad. Sci. U. S. A. 109, 10164–10168. https://doi.org/10.1073/pnas.1202473109.